Sub-10-nm electron-beam lithography for templated placement of colloidal quantum dots

by

Vitor Riseti Manfrinato

B.S., Electrical Engineering, University of Sao Paulo (2008)

Submitted to the Department of Electrical Engineering and Computer Science

in partial fulfillment of the requirements for the degree of

Master of Science in Electrical Engineering and Computer Science

at the

MASSACHUSETTS INSTITUTE OF TECHNOLOGY

September 2011

Signature of Author. .....
Department of Electrical Engineering and Computer Science
August 31st, 2011

Certified by. .....
Karl K. Berggren
Associate Professor of Electrical Engineering
Thesis Supervisor

Accepted by. .....
Leslie A. Kolodziejski
Chair, Department Committee on Graduate Students

Sub-10-nm electron-beam lithography for templated placement of colloidal quantum dots

by

Vitor Riseti Manfrinato

Submitted to the Department of Electrical Engineering and Computer Science on September 1, 2011, in partial fulfillment of the requirements for the degree of Master of Science in Electrical Engineering and Computer Science

Abstract

This thesis presents the investigation of resolution limits of electron-beam lithography (EBL) at the sub-10-nm scale. EBL patterning was investigated at low electron energy (2 keV) in a converted scanning electron microscope and at high electron energy (200 keV) in an aberration-corrected scanning transmission electron microscope. Sub-10-nm structures were fabricated and proximity effects were evaluated in both conditions.
As an application of sub-10-nm EBL, this thesis presents a templated-self-assembly technique to control the position of individual colloidal quantum dots smaller than 10 nm.

Thesis Supervisor: Karl K. Berggren
Title: Associate Professor of Electrical Engineering

Acknowledgements

First, I would like to thank my advisor, Prof. Karl Berggren, for the opportunity to work in his research group. I would like to further thank him for maintaining an exciting research environment, for providing an active mentorship, for sharing his research philosophy, for teaching countless communication techniques, and for his advice on writing techniques.

I would like to acknowledge the support from the Center for Excitonics, an Energy Frontier Research Center funded by the U.S. Department of Energy, Office of Science, Office of Basic Energy Sciences under Award Number DE-SC0001088.

There are many people that helped me in completing this thesis. I am very grateful to:

Dr. Huigao Duan for his guidance on the wonderful world of electron-beam lithography;

Prof. Jing Kong for the opportunity to first come at MIT as a visiting student and to discover a passion of life;

Prof. Marc Baldo for keeping a great research environment in the Center for Excitonics;

Prof. Henry Smith for advice on the fundamentals of nanofabrication;

Prof. Moungi Bawendi for his collaboration and valuable lessons of fundamental science;

Dr. Eric Stach for providing an excellent research environment at Brookhaven National Laboratory and for helpful discussions on transmission electron microscopy;

Prof. Alán Aspuru-Guzik for many discussions on energy research;

Prof. Terry Orlando and Prof. Leslie Kolodziejski for guidance on graduate student life;

Prof. James Fujimoto for mentorship and coursework guidance;

Mark Mondol for fundamental advice on electron-beam lithography and nanofabrication;

Jim Daley for maintain a professional research environment and for clean-room mentorship;

Dr. Yong Zhang for important advice on transmission electron microscopy;

Janet Fisher for advice on graduate student life;

Dr. Francesco Marsili for his friendship and mentorship on this thesis;

Lin Lee Cheong for her friendship, patience as collaborator, and useful discussions;

Jay-Byum Chang for his friendship and nanofabrication discussions;

Donald Winston for his friendship and charged-particle beam discussions;

Dr. Joel Yang and Dr. Bryan Cord for advice and discussions on electron-beam lithography;

Dr. Roman Caudillo, Katherine Harry, Sam Nicaise, Alejandro Perdomo-Ortiz, Javier Sanchez-Yamagishi, Dr. David Strasfeld, Dr. Sebastian Strobel, Dr. Dong Su, Darcy Wanger, Dr. Lihua Zhang for their patience as collaborators and for teaching me many lessons about science and engineering;

Labmates from the Quantum Nanostructures and Nanofabrication Group and NanoStructures Laboratory for their friendship;

Dr. Leonardo Campos and Dr. Paulo Araújo for priceless discussions on basic science and for teaching me the research way of life;

My friends from US and Brazil for moral support;
My family for believing in my work;
My parents, Wilson and Elza Manfrinato, and my sisters, Fernanda and Vivian Manfrinato, for believing in my work and for support.

Contents

1. Introduction.....14

1.1. Sub-10 nm electron-beam lithography.....14

1.2. Placement of colloidal quantum dots.....16

2. Sub-10 nm electron-beam lithography.....18

2.1. Low-energy electron beam lithography.....18

2.1.1. Introduction.....18

2.1.2. Methods.....19

2.1.3. Results.....22

2.2. STEM lithography.....31

2.2.1. Introduction.....32

2.2.2. Methods.....32

2.2.3. Results.....33

2.3. Summary 38

3. Quantum dot placement.....39

3.1. Fabrication process.....39

3.2. Process optimization.....40

3.3. Statistical analysis.....43

3.4. Surface chemistry.....45

3.5. Summary.....47

4. Future work.....48

4.1. Quantum dot optical characterization.....48

4.2. Sub-5 nm STEM lithography.....50

List of Figures

Figure 1-1. Schematic illustration of the resist exposure processes. The electron beam interacts with the resist generating elastic collisions, producing forward scattering, and inelastic collisions that produce secondary electrons. The secondary electrons can deposit energy through the resist leading to resist cross-linking or molecular scission required for exposure. Additionally, electrons can backscatter out of the resist. The initial electron spot size may limit minimum feature and, if broad enough, affects the minimum pitch (i.e., periodicity of dense features).....14

Figure 2-1. Scanning-electron micrographs of nested L's in 15-nm-thick HSQ exposed at 2 keV. (a) 9 nm half-pitch with a dose of 0.4 nC/cm (250 electrons/nm); (b) 10 nm half-pitch with a dose of 0.6 nC/cm (370 electrons/nm); (c) 15 nm half-pitch showing a clearly developed structure with a dose of 0.6 nC/cm (560 electrons/nm) (this experiment used cascading nested L's); (d) 20 nm half-pitch with a dose of 0.9 nC/cm (560 electrons/nm); and (e) 30 nm half-pitch with a dose of 1 nC/cm (620 electrons/nm).....23

Figure 2-2. Scanning-electron micrographs of a corner of a 4 μm × 4 μm dot array in 15-nm-thick HSQ, exposed at 2 keV. (a) 15 nm half-pitch with a dose of 2 fC/dot (12,000 electrons/dot) and (b) 13 nm half-pitch with a dose of 1.5 fC/dot (9,300 electrons/dot). The small deviation (~ 12 %) in dot diameter between the center and the corner of the array indicated minimal proximity effect.....24

Figure 2-3. The point-spread function (PSF) was obtained by plotting reciprocal dot dose versus the dot radius, followed by normalization (the maximum of the PSF was set to unity). (a) PSF for 15-nm-thick HSQ at 1.5, 2, 3 keV and 30 keV for 30-nm-thick HSQ; (b) PSFs of (a) for sub-60-nm radius. The 1.5 keV PSF had widest beam spreading at

sub-40-nm radius; (c) Experimental and Monte-Carlo-simulated PSFs at 2 keV, showing good agreement.....26

Figure 2-4. (a) Design of 2 μm × 2 μm patterned area with 40 nm × 40 nm unpatterned window at the center. (b) Normalized dose density (or aerial dose) calculated at the center of the unpatterned area, for low energy (2 keV) and high energy (30 keV). The exposure contrast at 2 keV is 5.5 times higher than at 30 keV.(c) Calculated process latitude (diameter variation versus hole diameter) of the pattern shown in (a), considering a 5% dose fluctuation. The process latitude is higher and the diameter variation is lower for 2 keV than at 30 keV.....29

Figure 2-5. Holes and trenches patterned in 15-nm-thick HSQ at 2 keV. (a) Pattern consisting of 2 μm × 2 μm exposed area with 40 nm × 40 nm unexposed windows at the center. (b) Scanning-electron micrograph of close-packed 30-nm-diameter holes in HSQ, using 10 nm step size and 0.3 fC/dot (1,860 electrons/dot). (c) Scanning-electron micrograph of 'EFRC' letters with a minimum feature size of 15 nm and minimal edge roughness.....31

Figure 2-6. Bright field transmission electron micrograph of 5-nm-half-pitch dot array of HSQ, exposed at 200 keV. The HSQ thickness was 20 nm and it was on top of a 50-nm-thick Si_3N_4 membrane. The dose was 9 fC/dot (54,000 electrons/dot).....34

Figure 2-7. The point-spread function (PSF) for 20-nm-thick HSQ at 30 keV and 200 keV. The PSF was obtained by plotting reciprocal dot dose versus the dot radius. The inset shows the fitting model for both PSFs. The fitting parameters were: $\alpha_{30\,keV} = 7.8$ nm; $\alpha_{200\,keV} = 4.3$ nm; $\gamma_{30\,keV} = 1.8$; and $\gamma_{200\,keV} = 1.1$.....35

Figure 2-8. Bright field transmission electron micrograph of HSQ structures exposed by the STEM at 200 keV. The HSQ thickness was 20 nm and it was on top of a 50-nm-thick Si_3N_4 membrane. The lines had a pitch of 15 nm, with feature size variation from 1 to 6 nm. The feature variation was due to different dwell times (electron dose) between dot and inter-dot exposures of the scanning beam (a beam blanker was not available). The HSQ structures appear to be fully developed, with some fallen-over posts indicated by slightly darker areas than the background.....37

Figure 3-1. (a) Fabrication process of templated QDs. PMMA was spin coated to a thickness of 40 nm on Si, followed by EBL. Then, 6 nm of CdSe QDs were spin coated. The PMMA lift off was done with acetone, leaving small clusters of CdSe QDs. (b) Scanning-electron micrographs of optimized PMMA templates with a minimum feature size of 8 nm for development at 7 °C.....40

Figure 3-2. Scanning-electron micrographs of templated 6-nm-diameter CdSe QDs generated by a solution with low (0.5 μM) (a)-(b) and high (2 μM) (c)-(d) concentration of QDs. The PMMA mask used was 40 nm thick. In (a) the QD clusters have from one to 10 QDs, with 25% pattern yield. (b) shows a cluster with two QDs from the sample shown in (a). (c) has from three to 15 QDs in each cluster, with 80% pattern yield. (d) is a sub-10 QD cluster from the sample shown in (c).....41

Figure 3-3. SEM micrographs of sub-10 nm holes in PMMA exposed by EBL at 30 keV, and developed for 30 s at: (a) 0°C; (b) 7°C; and (c) 15°C. (a) shows 8-9 nm holes. (b) has equal resolution than (a), and (c) shows larger features, i.e., 10-12 nm holes.....42

Figure 3-4. Scanning-electron micrographs of templated 6-nm-diameter CdSe QDs. The solution concentration was 2 μM. (a) shows an overview of the sample. There are a few

QDs present outside the patterned area. These QDs were presumably re-deposited during the lift-off process. (b) and (c) are higher magnification of the middle and bottom rows of QDs shown in (a). Clusters with one QD were achieved.....43

Figure 3-5. Histogram of the number of QDs (6-nm-diameter CdSe) in each cluster. The total number of analyzed clusters was 54. The QDs were counted visually by using high resolution SEM micrographs, obtained at 10 keV in a Zeiss SEM (Gemini column). Above every histogram bar is presented a typical SEM image used to count the QDs in a cluster.....44

Figure 3-6. Scanning electron micrographs of 4-nm-diameter CdSe/CdZnS spun on SiO_2 substrates. (a) shows QDs purified one time without further processing. (b) shows QDs as prepared in (a) followed by acetone dipping for 3 min to simulate the lift-off conditions of the QD-patterning process. (c) consists of QDs purified three times without further processing. (d) consists of QDs as prepared in (c) followed by acetone dipping for 3 min. The insets of all figures show higher magnification of the darker areas, which are QD agglomerations. The QD attachment after acetone processing is clearly improved with three purification steps, which indicate the smaller concentration of ligands on QD surface favors its adhesion on the substrate.....46

Figure 4-1. Confocal photoluminescence (PL) of CdSe QDs with 6 nm diameter. The peak of emission wavelength was 540 nm. This large area pattern maintained its PL even two weeks after the fabrication process, in ambient atmosphere. However, the sub-20nm clusters of QDs did not presented PL.....49

Figure 4-2. Confocal photoluminescence of CdSe/CdZnS QDs (core/shell with 4nm core) with 9 nm diameter. The peak of emission wavelength was 610 nm. These QDs were templated, but there was significant re-deposition of QDs. Nevertheless, these small clusters of QDs maintained PL, i.e., they are optically active after the fabrication process.....50

Figure 4-3. Bright field transmission electron micrograph of HSQ lines, exposed at 200 keV. The HSQ thickness was 20 nm and it was on top of a 50-nm-thick Si_3N_4 membrane. (a)-(c) had linear-dose of 17 nC/cm (11,000 electrons/nm), 30 nC/cm (19,000 electrons/nm), and 50 nC/cm (31,000 electrons/nm), respectively. The exposure step size was 2 nm. (a) did not receive enough dose in the entire line and collapsed. In addition, there is significant proximity effect generated by the exposed pads connected to the lines, indicated by the larger width at the beginning and end. (b) had non-uniform line-width, with 2.5 nm as minimum width at the center. (c) had sufficient dose and better uniformity than (a) and (b).....51

Figure 4-4. Schematic top-view of a structure to avoid collapse during development. Blue area represents the fabricate structure and the white background is the substrate. The large area pads and reinforced interconnects in this grating are designed to give mechanical stability to the thin lines that compose the square grating.....52

Chapter 1. Introduction

1.1. Sub-10 nm electron-beam lithography

Electron-beam lithography (EBL) readily enables sub-10 nm resolution[1-4]. EBL has been used through many decades[5], but its resolution limits at the sub-10-nm scale were not thoroughly investigated. Resolution limiting factors to be addressed are spot size, electron scattering, secondary electron range, resist development, and resist chemical and mechanical structure. Figure 1-1 illustrates the main limiting factors on the exposure process. Unfortunately, these limiting factors are not easily separable, leading to a challenging analysis. Therefore, understanding the effect of these individual limiting factors and the correlation between them is fundamental to drive EBL to the atomic scale of resolution.

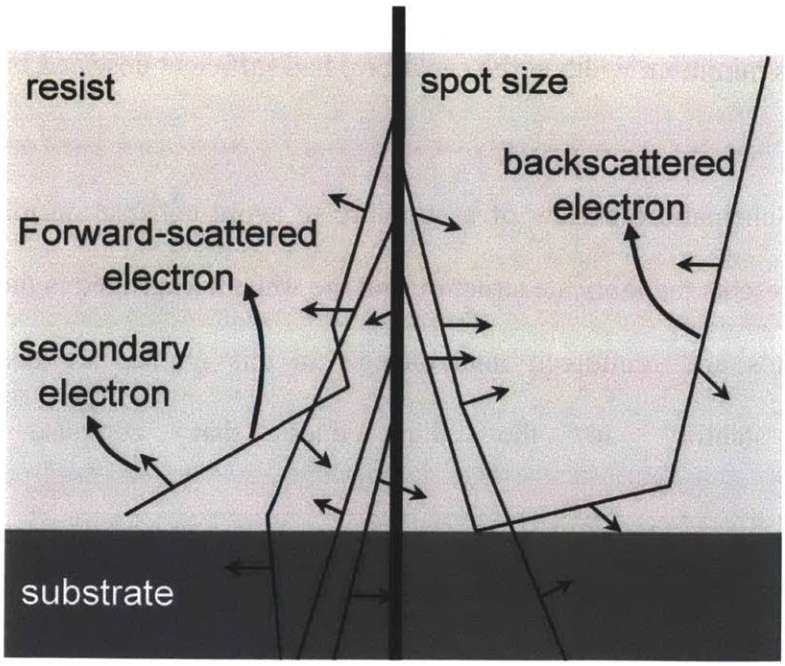

Figure 1-1. Schematic illustration of the resist exposure processes. The electron beam interacts with the resist generating elastic collisions, producing forward scattering, and inelastic collisions that produce secondary electrons. The secondary electrons can deposit energy through the resist leading to resist cross-

linking or molecular scission required for exposure. Additionally, electrons can backscatter out of the resist. The initial electron spot size may limit minimum feature and, if broad enough, affects the minimum pitch (i.e., periodicity of dense features).

Many approaches have been used to investigate these EBL limiting factors, such as: investigating different resists[6-8], varying electron beam spot size[9]; varying electron energy to change electron-matter interaction[10], optimizing resist processing of pre and post exposure, optimizing resist development[2,11,12], and simulating the deposited energy into resist[13-15]. Nevertheless, from a resolution perspective, resist-based lithography was limited to ~ 4 nm features and ~ 16 nm pitch[16] (i.e., periodicity of dense features).

The current EBL resolution limit is further complicated by the reduced length scale. Since feature size was decreased to below 10 nm, patterning metrology becomes a major limiting factor for conventional scanning electron microscopy (SEM). To overcome this limitation, more accurate tools are necessary for metrology, such as the transmission electron microscope (TEM) and atomic force microscope (AFM)[16].

Another complication of EBL at the sub-10 nm scale is mass-transport limitations during development. Resist development of dense features poses a challenge because chemical reactions and transport of developer species became sensitive to feature dimension and density[3, 4, 16]. This problem demands understanding of resist development at the atomic scale and will require sophisticated development solutions.

This thesis focus on two major resolution limiting factors: (1) electron scattering, and (2) spot size. The electron scattering will be investigated by varying electron energy of the electron beam, thus changing electron-matter interactions and the deposited energy into resist. The electron energy range explored was from 1 to 5 keV in a converted-SEM

(Raith150) EBL system and 200 keV in an aberration-corrected scanning transmission electron microscope (STEM). The spot size was ~ 8 nm for the converted SEM[3] and 0.15 nm for the STEM[17]. In addition, this thesis presents analysis of proximity effect for low (sub-5 keV) and high-energy (200 keV) EBL and correspondent applications. The resist type and developer system were chosen to maximize resolution and minimize their effects on the previously mentioned limiting factors. The resist used was hydrogen silsesquioxane due to its high resolution capabilities demonstrated over the past 5 years[1, 2, 11]. The resist development used was salty development because of its high dose contrast.

1.2. Placement of colloidal quantum dots

Sub-10-nm EBL is key to nanoscience research, such as in emerging fields of excitonics,[18] plasmonics,[19] and nano-optics[20]. One application of sub-10-nm patterning is in fabricating excitonic and nano-optical devices by using semiconductor colloidal quantum dots (QDs).

Semiconductor QDs are important building blocks for nanoscience[21]. One key aspect of such system is the fine control of optical transitions in the synthesis process[22]. Another QD feature is their atom-like behavior due to discrete energy levels.

For convenience, QDs are predominantly used in a thin-film arrangement, deposited by spin casting or dip coating. This ensemble configuration of QDs is extensively used to investigate fundamental properties of this system, such as band gap engineering,[22] energy transfer,[23-25] and multi-exciton generation[26]. Important applications are possible in this ensemble arrangement, such as QD solar cells[26] and QD light-emitting diodes[27].

However, the investigation of single QDs, dimers (two QDs), and trimers (three QDs) is limited by complex[28] and non-reproducible processes. Therefore, single-QD patterning is one of the major challenges to both investigate and design a system that takes advantage of individual properties of QDs[20]. Previous reports have demonstrated placement of sub-100-nm clusters of gold colloidal QDs,[12, 29-32] and semiconductor colloidal QDs[33-36]. However, further investigation is necessary for the placement of single semiconductor QDs smaller than 10 nm.

Applications that may emerge by using this technique are the fabrication of single-photon emitters,[20, 37] excitonic circuits,[38-40] and nano-optical devices[41].

This thesis presents a templated-self-assembly technique to control the position of individual QDs by using sub-10 nm EBL.

Chapter 2. Sub-10 nm electron-beam lithography

Sub-10-nm electron-beam lithography (EBL) is fundamental for the placement of colloidal quantum dots (QDs) smaller than 10 nm. Important characteristics from EBL are resolution, pattern uniformity, and throughput.

This chapter describes the investigation of resolution limits, dose requirements, and proximity effects of low-energy (sub-5 keV) and high-energy (200 keV) EBL. These EBL techniques would be ultimately applicable in the placement of single QDs smaller than 10 nm.

2.1. Low-energy EBL

This section is dedicated to the resolution limits and proximity effects of sub-5 keV EBL.

2.1.1. Introduction

Electron-beam lithography at energies 30 keV and above is a well established method of fabricating sub-20-nm-pitch structures[1, 3, 4]. However, EBL at these high energies suffers from long-range proximity effects. Low-energy (sub-5 keV) EBL exhibits five key advantages over EBL at higher energies: (1) reduced dwell-time required for exposure (due to a higher resist sensitivity with only slightly reduced beam current)[42-44]; (2) lower system cost and a smaller footprint[44, 45]; (3) significant reduction in long-range proximity effects[6, 42, 44]; (4) lower probability of sample damage and substrate heating; and (5) more efficient delivery of energy into ultra-thin resists and self-assembled monolayers[46].

Previously, the finest pitch reported for adjacent lines fabricated at beam energies below 5 keV was 50 nm using calixarene[47], 60 nm using ZEP-7000[47], 50 nm using poly-

methyl-methacrylate (PMMA)[48], and 60 nm using hydrogen silsesquioxane (HSQ)[49]. This range of resolution is not sufficient for applications that require high throughput and high pattern resolution, such as photomask fabrication and multiple-electron-beam lithography for integrated circuits[44]. The key challenges to achieving high resolution at low electron energies are the reduced electron range, the increased broadening of the incident beam (forward-scattering), and larger minimum spot size. To overcome these limitations, our experiments were conducted with ultra-thin (~ 15-nm-thick) HSQ in conjunction with high-contrast development.

Monte-Carlo models of electron scattering at sub-5 keV[14, 15, 50] have never been tested at sub-20 nm length scales. The validity of low-energy exposure models are thus an important question in the field.

This thesis presents the fabrication of 9 to 30-nm-half-pitch nested-L structures, and 13- and 15-nm-half-pitch dot arrays at electron energy of 2 keV. The dots at the corners of the 4 μm × 4 μm arrays showed minimal deviation in diameter, indicating minimal long-range proximity effect. Monte-Carlo simulations of the point-spread function (PSF) at low electron energies are in agreement with experimental results. To demonstrate the expected reduced long-range proximity effect, we exposed a 2 μm × 2 μm area in HSQ, leaving a small central region unexposed. This type of structure would be extremely difficult to realize (even with proximity-effect correction) at higher energies.

2.1.2. Methods

The resolution of low-energy EBL is expected to be lower than that of high-energy EBL (e.g. 30 keV to 200 keV) due to increased electron scattering and generally larger spot

size. In addition, the dose required to expose HSQ at low energies should also be much lower due to more efficient energy-transfer between the incoming electrons and the resist[43].

To experimentally determine the resolution limit of low-energy EBL, all samples were prepared by spin-coating HSQ (1% solids XR-1541, Dow Corning) on silicon wafers (p-type Boron doped, 10-25 Ω.cm) with native silicon dioxide at a spin-speed of 6.5 krpm. The resulting thickness was determined to be 15 nm using an ellipsometer. To avoid thermally-induced cross-linking of HSQ, which might lead to a loss in resolution, no pre-exposure bake was performed[2]. Unless stated otherwise, all exposures in this section were carried out at an electron energy of 2 keV on a Raith 150 EBL system with a thermal-field-emitter source operating at 1800 K (~ 0.5 eV energy spread), a 20 μm aperture, 50 μm field size, a working distance of 6 mm and a beam current of 64 pA. After exposure, samples were immersed in salty developer[2] for 4 min at 24°C, rinsed under deionized water for 2 min, and blown dry with nitrogen gas. The typical total processing period from spin coating to development was about 2-3 days. The fabricated structures were imaged by scanning-electron microscope (SEM) at 10 keV with ~ 6 mm working distance, and their dimensions were measured by using commercial image processing software (ImageJ).

In high-energy (e.g., 30 keV to 100 keV) EBL, a large background dose extends over several micrometers, due to back-scattered electrons. This long-range proximity effect is expected to be much less severe at low-energies due to the shorter electron range. However, this expectation had never been verified at length scales smaller than 50 nm, which is of ever-increasing importance in direct-write lithography.

We measured the point-spread function (PSF) at energies of 1.5, 2, and 3 keV. Isolated dots were patterned in 15-nm-thick HSQ with single-pixel exposures with doses ranging from 0.1 fC/dot (6×10^3 electrons) to 10^5 fC/dot (6×10^9 electrons), followed by salty development[2]. The radii of the dots were measured from SEM micrographs using image processing software (ImageJ), as described in Ref. 51 The reciprocal dot dose was then plotted versus the dot radius, and each PSF was normalized.

To evaluate proximity effect advantages at low-energy EBL, the normalized dose density (charge per unit area) was calculated. A 2 μm × 2 μm exposed area was divided into an address grid of 10 nm pitch (i.e., 200 × 200 address points) with 4 × 4 unexposed points at the center. For each point at position (x, y) in the structure, the distance $d(x, y; n, m)$ to every exposed point at position (n,m) in the array was calculated:

$$d(x, y; n, m) = \sqrt{|x - n|^2 + |y - m|^2}.$$

For this calculation we considered radially symmetric PSFs[52]:

$$PSF(r, \theta) = PSF(r)\,.$$

In order to easily manipulate the PSFs for dose distribution calculations, a fitting function was obtained for each PSF. Typically double Gaussians are used as fitting functions. However, such fitting functions are not accurate for beam energies from 2 to 30 keV. For the 2 keV PSF, we used three Gaussian functions and achieve a close fit of the PSF in the measured range. For the 30 keV PSF, we used two Gaussians plus a hyperbolic function. The physical meaning of the fitted functions is not studied in this work. Because the hyperbolic function goes to infinity for radii close to zero and we do not have any data on the 30 keV PSF for distances less than 10 nm, the hyperbolic function is only applied at 10 nm and above and goes to zero below 10 nm. The fitting

parameters for the functions are provided in[53].

As described by Ref. 52, we used the aforementioned experimentally fitted PSFs to calculate the contribution to the dose density $\delta(x,y)$ from every exposed point (with charge Q):

$$\delta(x,y) = Q\sum_{n,m} PSF\big(d(x,y;n,m)\big).$$

2.1.3. Results

Two designs of nested-L test structures, consisting of either five or seven single-pixel L-shaped-lines, were patterned in 15-nm-thick HSQ at half-pitches from 9 to 30 nm. Figure 2-1 shows nested L's at half-pitches of 9, 10, 15, 20, and 30 nm (the 15-nm-half-pitch structure was fabricated in a separate experiment in Ref. 54). Although the 9- and 10-nm-half-pitch structures could be resolved, residual HSQ was present between the lines, and the single isolated lines were washed away. On the other hand, structures patterned at 15, 20 and 30 nm half-pitches appeared to be fully developed.

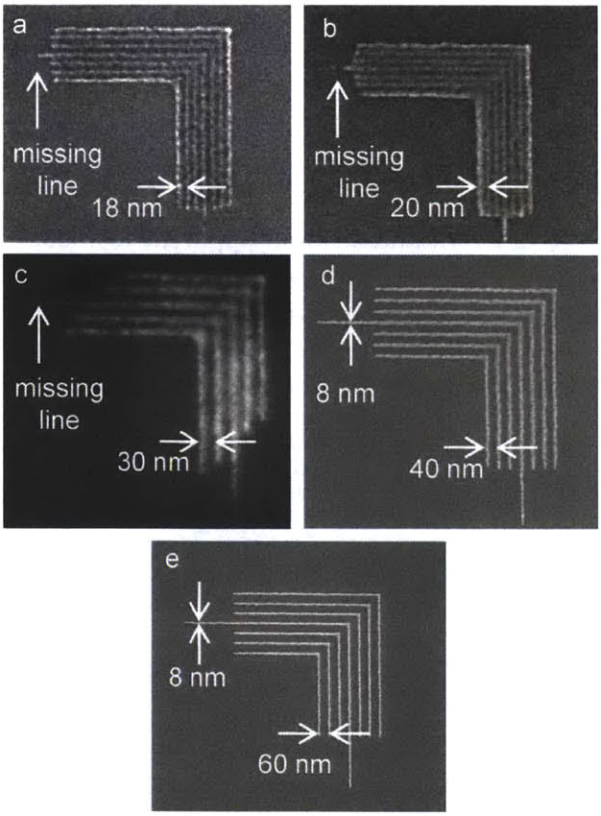

Figure 2-1. Scanning-electron micrographs of nested L's in 15-nm-thick HSQ exposed at 2 keV. (a) 9 nm half-pitch with a dose of 0.4 nC/cm (250 electrons/nm); (b) 10 nm half-pitch with a dose of 0.6 nC/cm (370 electrons/nm); (c) 15 nm half-pitch showing a clearly developed structure with a dose of 0.6 nC/cm (560 electrons/nm) (this experiment used cascading nested L's); (d) 20 nm half-pitch with a dose of 0.9 nC/cm (560 electrons/nm); and (e) 30 nm half-pitch with a dose of 1 nC/cm (620 electrons/nm).

As previously suggested,[6] by using the ultra-thin resist we reduced the impact of forward scattered electrons, leading to higher resolution than seen previously[44, 49]. In addition, the use of HSQ with high-contrast development aided in achieving higher resolution. The minimum half-pitch observed (9 nm) coincided with the electron beam spot size (9 nm), which was measured previously in Ref. 3.

To evaluate if we could maintain high resolution over large areas, we exposed 4 μm × 4 μm dot arrays on 15-nm-thick HSQ at 2 keV, with half-pitches of 15 nm and 13

nm (~ 1 Teradot/in.^{2} or ~ 0.15 Teradot/cm^2), as shown in Figures 2-2a and 2-2b, respectively. A small amount of residual HSQ was present between the 13-nm-half-pitch dots, and the dots had considerable variation in diameter. In contrast, the dots in the 15-nm-half-pitch array were uniform and without apparent residual HSQ between the dots. The dots at the corner of the array showed only minimal size deviation (~ 12 %), demonstrating that the long-range proximity effect was minimal, as expected.

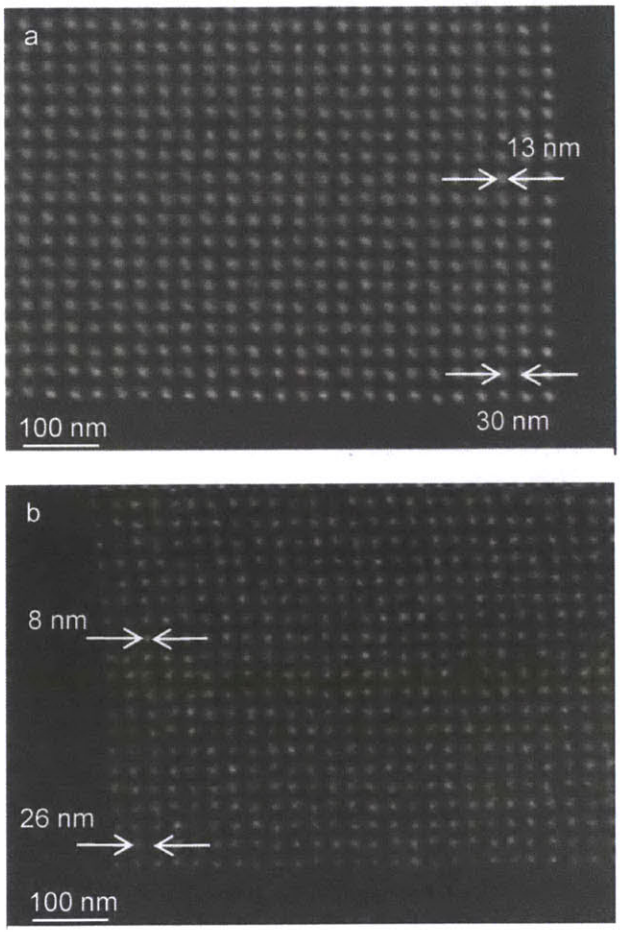

Figure 2-2. Scanning-electron micrographs of a corner of a 4 μm × 4 μm dot array in 15-nm-thick HSQ, exposed at 2 keV. (a) 15 nm half-pitch with a dose of 2 fC/dot (12,000 electrons/dot) and (b) 13 nm half-pitch with a dose of 1.5 fC/dot (9,300 electrons/dot). The small deviation (~ 12 %) in dot diameter between the center and the corner of the array indicated minimal proximity effect.

Patterning the same structures as shown in Figure 2-1 at 30 keV required 6.4 (4,000 electrons/nm) to 16 nC/cm (9,900 electrons/nm), which is roughly 16 times higher than what was required at 2 keV. The increased resist sensitivity at low energies may pose problems for more sensitive resists such as PMMA by causing shot noise and increased line-edge roughness[55].

The PSF (i.e., spatial distribution of deposited energy into resist) was measured to evaluate proximity effects. Figure 2-3a compares the experimental PSFs we obtained with the PSF at 30 keV, determined in Ref. 56 in 30-nm-thick HSQ.

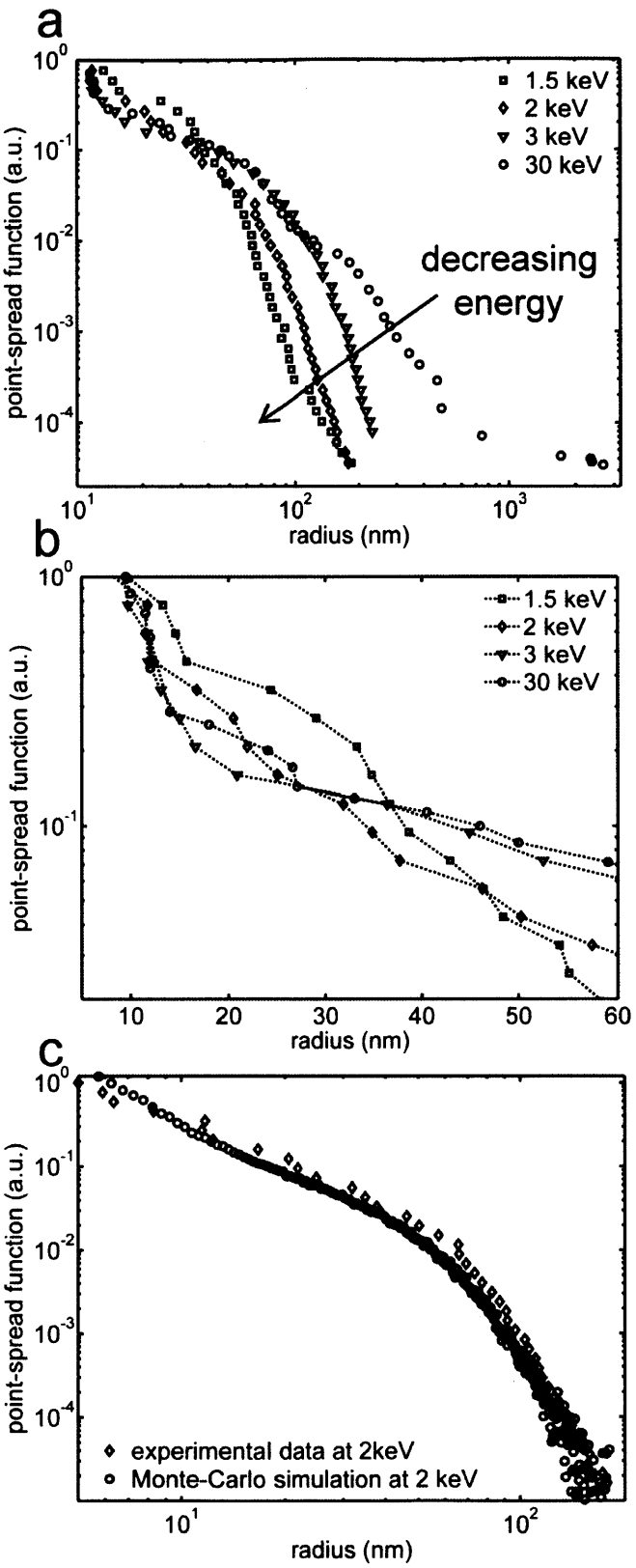

Figure 2-3. The point-spread function (PSF) was obtained by plotting reciprocal dot dose versus the dot

radius, followed by normalization (the maximum of the PSF was set to unity). (a) PSF for 15-nm-thick HSQ at 1.5, 2, 3 keV and 30 keV for 30-nm-thick HSQ; (b) PSFs of (a) for sub-60-nm radius. The 1.5 keV PSF had widest beam spreading at sub-40-nm radius; (c) Experimental and Monte-Carlo-simulated PSFs at 2 keV, showing good agreement.

For PSF comparison in the long-range (radius bigger than 40 nm), we defined an effective electron range, which is as a point where the dose is 10^{-5} smaller than the incident dose. At this range, the deposited dose is considered negligible for all practical purposes. As shown in the Fig. 2-3a, this effective range of the electrons at 1.5 and 2 keV is less than 200 nm. Figure 2-3b is a magnified view of the same PSFs at radii 60nm and below. The PSFs at 2, 3 and 30 keV are approximately the same for the short range (radius smaller than 40 nm), presumably due to the use of thin resist. Only the 1.5 keV PSF has somewhat wider beam-spreading at this short range.

A Monte-Carlo simulation based on Refs. 14, 15, 50 was conducted to determine if the measurements were in agreement with the modified Bethe energy dissipation law for low energies. We assume that the high contrast of HSQ with salty development (contrast value, $\gamma = 10$) permits a direct comparison between the experimental and simulated PSFs. We also assume that the dose distribution of the Monte-Carlo simulation represents a close approximation to the cross-linking distribution. The experimentally determined and simulated PSFs are in good agreement for energies 1.5, 2, and 3 keV. Figure 2-3c is a plot of the simulated and experimental PSFs at 2 keV.

There are several possible hypotheses that could explain the small observed mismatch between simulated and experimental PSFs, seen in Figure 2-3c. The high but finite contrast of the salty developer causes a broadening in the PSF, as observed at large

radius. Mass-transport limitation during development[16] is a possible source of experimental deviation at the sub-20 nm scale. SEM metrology is also imperfect, particularly for dots with small radius, i.e. sub-20 nm dots are expected to have proportionally larger errors in the PSF measurement.

To demonstrate the reduced scattering range at low energies, we simulated the pattern in Figure 2-4a and exposed the pattern shown in Figure 2-5a. These patterns are illustrative of and sensitive to long-range proximity effects. If the background dose in the unexposed area is less than the threshold required for HSQ to cross-link, then a hole will be present. However, if the proximity effect is substantial, the hole will be exposed by the scattered electrons.

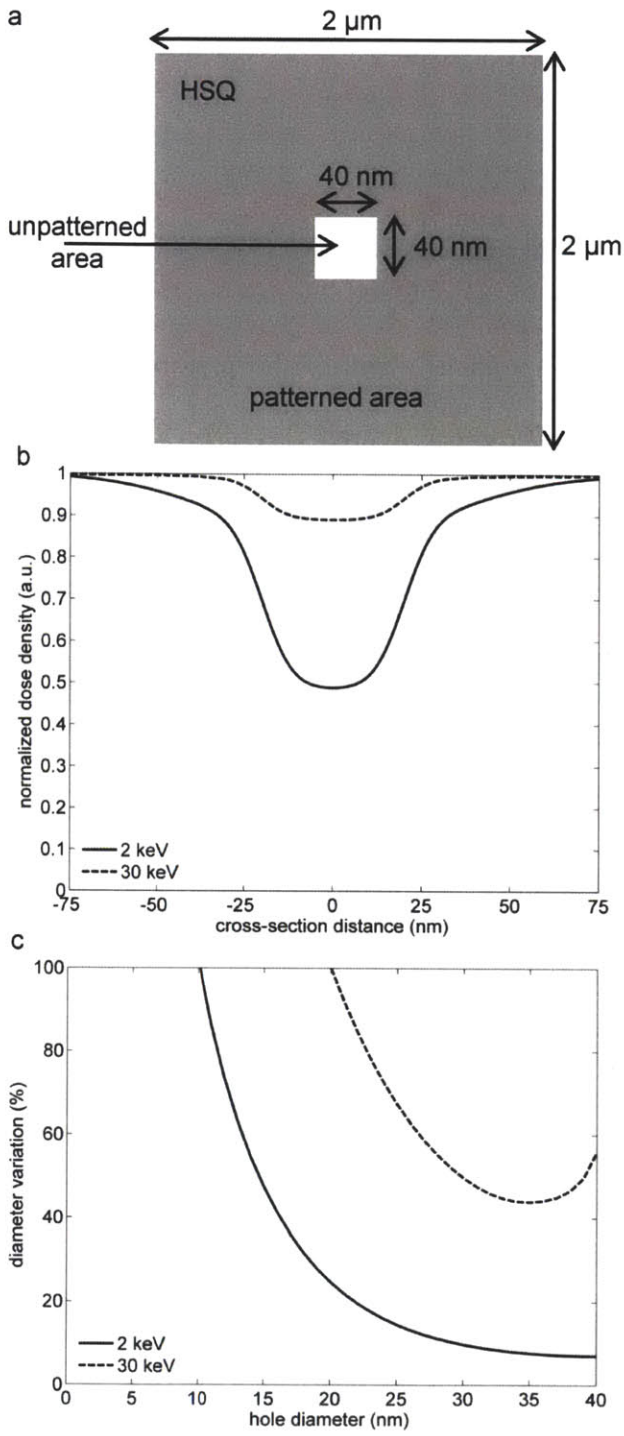

Figure 2-4. (a) Design of 2 μm × 2 μm patterned area with 40 nm × 40 nm unpatterned window at the center. (b) Normalized dose density (or aerial dose) calculated at the center of the unpatterned area, for low energy (2 keV) and high energy (30 keV). The exposure contrast at 2 keV is 5.5 times higher than at 30 keV.(c) Calculated process latitude (diameter variation versus hole diameter) of the pattern shown in (a),

considering a 5% dose fluctuation. The process latitude is higher and the diameter variation is lower for 2 keV than at 30 keV.

Figure 2-4b shows the normalized doses density (charge per unit area) calculated at the center of the pattern shown in Figure 2-4a for electron energies of 30 keV and 2 keV. Exposure contrast K was used to quantify the proximity effects at the center of the pattern. K was defined as $(Dose_{\max} - Dose_{\min})/(Dose_{\max} + Dose_{\min})$, where $Dose_{\max}$ was the maximum dose in the entire pattern and $Dose_{\min}$ was the minimum dose in the unexposed central region of the pattern. As shown in Figure 2-4b, the background dose at 2 keV is much lower than that at 30 keV. K = 0.06 for 30 keV and 0.33 for 2 keV.

We also calculated the process latitude for this pattern at 2 and 30 keV, shown in Figure 2-4c. For holes from 0 to 40 nm diameter, a dose variation of 5% was considered. Such dose variation translates into a variation in hole diameter. Figure 2-4c shows a better process latitude for 2 keV exposures than at 30 keV exposures due to the reduced long-range proximity effect. For a hole with 30 nm diameter, the 2 keV exposure has ~ 10% diameter variation while the 30 keV exposure has ~ 50% diameter variation.

To experimentally confirm the dose simulation we exposed the pattern in Figure 2-5a. Figure 2-5b is a SEM micrograph of the fabricated pattern in the HSQ. The holes were 30 nm in diameter. A more complex pattern, spelling the letters 'EFRC', was also fabricated (Fig. 2-5c) with features at the 20 nm length scale.

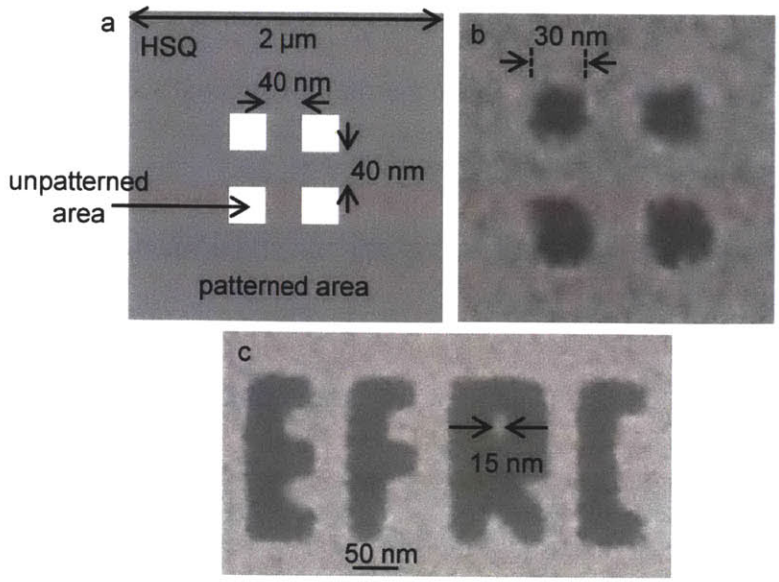

Figure 2-5. Holes and trenches patterned in 15-nm-thick HSQ at 2 keV. (a) Pattern consisting of 2 μm × 2 μm exposed area with 40 nm × 40 nm unexposed windows at the center. (b) Scanning-electron micrograph of close-packed 30-nm-diameter holes in HSQ, using 10 nm step size and 0.3 fC/dot (1,860 electrons/dot). (c) Scanning-electron micrograph of 'EFRC' letters with a minimum feature size of 15 nm and minimal edge roughness.

A drawback of using low-energy EBL is the difficulty in patterning thick resists. The finite penetration depth of low-energy electrons limit the maximum resist thickness possible, and forward scattering reduces resolution as the resist thickness increases[6]. The use of bi-layer or tri-layer stacks becomes necessary. Transferring high resolution patterns from resist to an underlying material is a concern due to the thinness of the electron-beam resist. Fortunately, HSQ provides better etch resistance compared to organic resists, such as poly(methylmethacrylate) (PMMA).

2.2. STEM lithography

This subsection focuses on the resolution limits and short-range proximity effects of 200 keV EBL, which was carried out with an aberration-corrected scanning transmission electron microscope (STEM) as the exposure system.

2.2.1. Introduction

The known resolution limiting factors of EBL are[3]: primary-electron scattering, spot size, secondary electron range, development process, and resist structure. We decided to minimize the influence of electron scattering and spot size to facilitate the resolution limit analysis. To minimize primary-electron scattering, we chose an exposure with 200 keV electrons. To minimize the spot size, we chose an aberration-corrected STEM as the exposure system, featuring a 0.15 nm spot size with beam current of 150 pA[17].

STEM exposures have been done before in conventional resists, such as poly(methyl methacrylate) (PMMA)[57]and calixarene[58], and in low-molecular-weight resists, such as NaCl[59]. The minimum feature in PMMA was 3-5 nm and 30 nm pitch. The minimum feature in NaCl was 1.5 nm and 4.5 nm pitch, but with the drawback of 500 times smaller sensitivity than PMMA. Nevertheless, the resolution-limiting factors were not systematically explored in these studies.

This thesis present an analysis of the resolution limits at sub-10 nm scale by using recently developed processing[2] and metrology method[16].

2.2.2. Methods

To experimentally determine the resolution limit of 200 keV EBL, all samples were prepared by spin-coating HSQ (1% solids XR-1541, Dow Corning) on 50-nm-thick Si_3N_4

membranes at a spin-speed of 6 krpm. The resulting thickness was ~20 nm, measured by fallen over structures on TEM. To avoid thermally-induced cross-linking of HSQ, which might lead to a loss in resolution, no pre-exposure bake was performed[2]. The exposures were carried on a Hitachi HD 2700C aberration-corrected STEM (at Brookhaven National Laboratory) with a cold-field-emitter source (~ 0.3 eV energy spread) and a beam current of 100-150 pA. After exposure, samples were immersed in salty developer[2] for 4 min at 24°C, rinsed under deionized water for 2 min, rinsed in isopropyl alcohol for 15 s, and blown dry with nitrogen gas. The typical total processing period from spin coating to development was about 4 days. The fabricated structures were imaged using a JEOL 2010F transmission electron microscope (TEM) at 200 keV, and their dimensions were measured by image processing software (ImageJ).

The point-spread function (PSF) of this 200 keV EBL system was measured to analyze the resolution limits and proximity effect at the sub-60 nm length scale. To measure the PSF at 200 keV, isolated dots were patterned in 20-nm-thick HSQ with single-pixel exposures with doses ranging from 1 fC/dot (6×10^4 electrons/dot) to 10^3 fC/dot (6×10^7 electrons/dot), followed by salty development[2]. The radii of the dots were measured from TEM micrographs using commercial image processing software (ImageJ). The reciprocal dot dose was then plotted versus the dot radius, as described in Ref. 51.The PSF was normalized and compared to a 30 keV PSF measured in Ref. 16.

2.2.3. Results

Figure 2-6 shows a HSQ dot array with 5 nm half-pitch, which was the minimum half-pitch achieved. There was no observed resist residue between the dots after development.

This result represents a significant improvement over previous reports at 30 keV[2, 16]. To understand this improvement, the point-spread function (PSF) was measured at 200 keV.

Figure 2-7 shows the measured PSF at 200 keV and the PSF at 30 keV from Ref. 16. It is clear that the 200 keV PSF is sharper than at 30 keV. The functional model of these PSFs is shown on the inset of Figure 2-7. The range of forward scattered electrons is represented by the α parameter in the fitted PSFs. The $\alpha_{30\ keV}$ was 7.8 nm and $\alpha_{200\ keV}$ was 4.3 nm, which is 1.8 times smaller. In addition, the difference in the proximity effect within this sub-60 nm range was quantified. The volumetric distributed dose (charge per volume) at 200 keV was 37% smaller than at 30 keV, representing a significant reduction in short-range proximity effect.

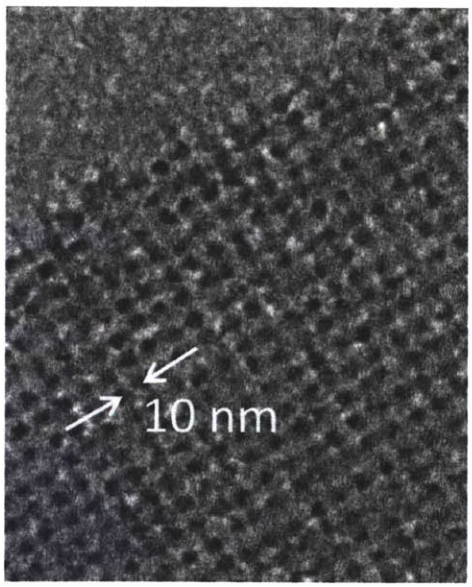

Figure 2-6. Bright field transmission electron micrograph of 5-nm-half-pitch dot array of HSQ, exposed at 200 keV. The HSQ thickness was 20 nm and it was on top of a 50-nm-thick Si_3N_4 membrane. The dose was 9 fC/dot (54,000 electrons/dot).

We considered the following limiting factors to pattern this 5-nm-half pitch structure: spot size; mass-transport limitation during development; and proximity effect (i.e., electron scattering). The spot size was not a limiting factor for the minimum pitch because it is significantly smaller than the minimum half-pitch. In addition, the development process was sufficient to fully develop the structure. Thus, the reduced short-range proximity effect was the main factor that resulted in higher resolution than the previous report at 30 keV.

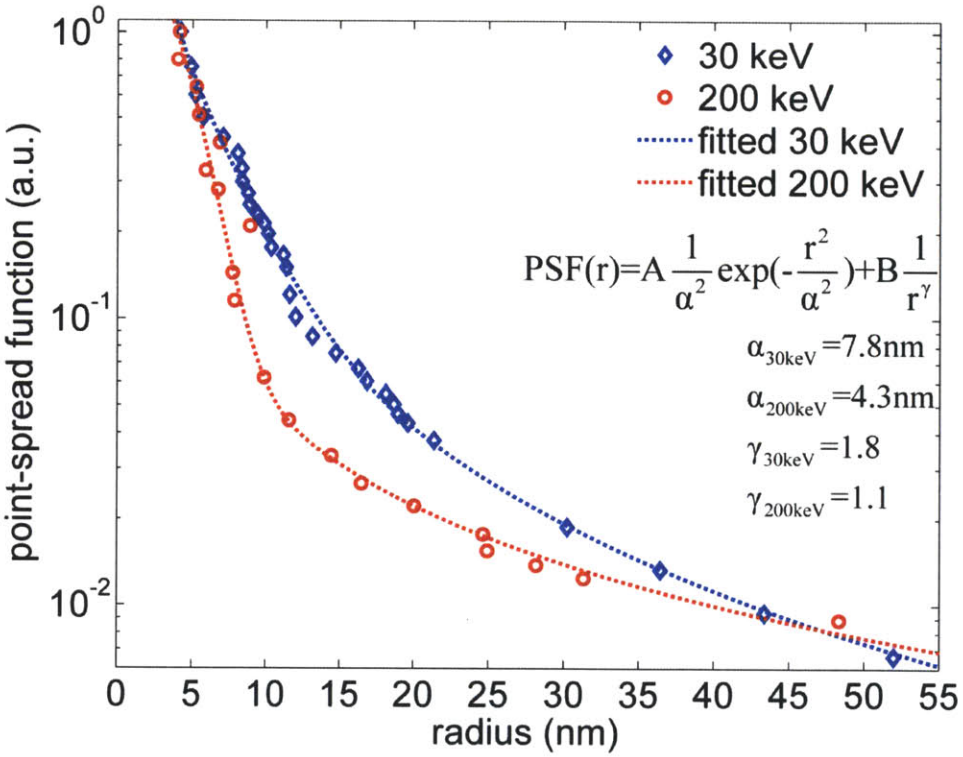

Figure 2-7. The point-spread function (PSF) for 20-nm-thick HSQ at 30 keV[16] and 200 keV. The PSF was obtained by plotting reciprocal dot dose versus the dot radius. The inset shows the fitting model for both PSFs. The fitting parameters were: $\alpha_{30\,keV}$ = 7.8 nm; $\alpha_{200\,keV}$ = 4.3 nm; $\gamma_{30\,keV}$ = 1.8; and $\gamma_{200\,keV}$ = 1.1.

The electron dot dose to expose the structure in Figure 2-6 was 9 fC. This dot dose is the same for 30 keV exposures, which is counterintuitive according to the Bethe

equation. One hypothesis for this dose mismatch is a resist heating effect. The current density in the used STEM was ~ 600 times higher than in a conventional 30 keV EBL system. Therefore, more joule heating is expected with STEM exposure which could shift the resist sensitivity. Nevertheless, more experiments are necessary to validate this hypothesis, such as verifying the sensitivity at different current densities.

The minimum feature size attainable with HSQ at 200 keV was also investigated. A dot array was fabricated with 15 nm pitch, but slightly overdosed. Figure 2-8 shows the resultant array with HSQ structures down to 1 nm. This preliminary result gave the smallest resist structure ever written by EBL in conventional resists. This result was only achieved by the combined use of sub-nm spot size, proper STEM stability (high electron beam current for STEM - 150 pA - and small sample drift – ~ 1 nm/min), high-contrast development (contrast value, γ = 10), high-resolution capabilities of HSQ, and sub-nm metrology obtained with TEM.

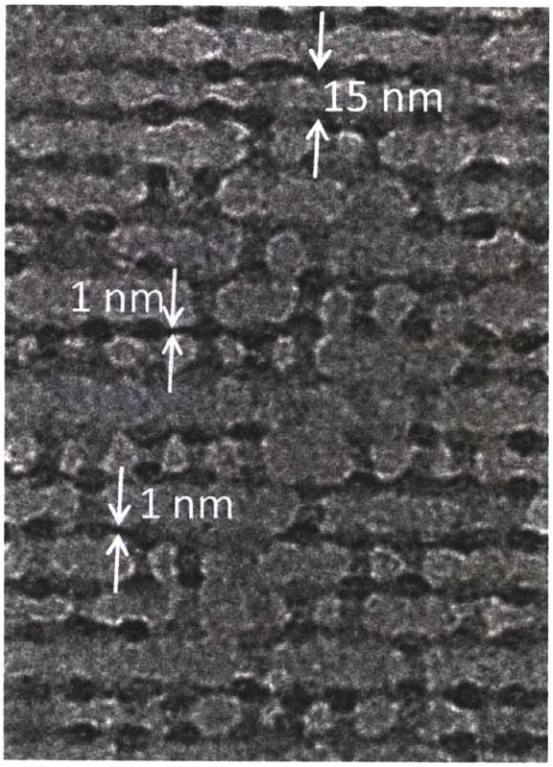

Figure 2-8. Bright field transmission electron micrograph of HSQ structures exposed by the STEM at 200 keV. The HSQ thickness was 20 nm and it was on top of a 50-nm-thick Si_3N_4 membrane. The lines had a pitch of 15 nm, with feature size variation from 1 to 6 nm. The feature variation was due to different dwell times (electron dose) between dot and inter-dot exposures of the scanning beam (a beam blanker was not available). The HSQ structures appear to be fully developed, with some fallen-over posts indicated by slightly darker areas than the background.

Aberration-corrected STEM lithography has also a throughput advantage. Such a microscope provides high electron-beam current (up to 200 pA in existing tools) with sub-Angstrom spot size. Such features are not available in standard EBL tools. For instance, the beam current of an electron optics column (e.g., scanning electron microscope) is proportional to the square power of spot diameter[60]. Considering this assumption to be valid for our STEM system (0.15 nm spot at 200 pA), one could obtain

a 2 nm spot size with beam current of 35 nA. Thus, the use of aberration corrector might lead to ~ 10 times higher throughput than existing EBL tools for sub-5 nm patterning.

2.3. Summary

We have shown that low-energy EBL is capable of patterning with high resolution and a significantly reduced exposure dose. A resolution limit of 15-nm-half-pitch for nested L's and large-area dot array in HSQ was achieved at 2 keV. We also fabricated 9-nm-half-pitch nested L's and 13-nm-half-pitch large-area dot array, but resist residues were observed. The required dose at 2 keV was about one order of magnitude lower compared to that required at 30 keV. PSFs at low energies were experimentally determined and were in good agreement with Monte-Carlo simulations. From the experimental PSFs, the effective scattering range of electrons at energies 1.5 and 2 keV was less than 200 nm. The long-range proximity effects at sub-5-keV are much lower than at 30 keV, as demonstrated in the 'hole-in-HSQ' structures and the minimal dot diameter deviation at the corners of the large dot arrays.

We have also shown that 200 keV EBL is capable of patterning HSQ structures with 5 nm half-pitch and 1 nm minimum feature size. In addition, the smaller short-range proximity effect at 200 keV was the main reason for achieving higher resolution than at 30 keV.

Chapter 3. Quantum dot placement

This chapter describes a templated-self-assembly technique developed to control the position of individual colloidal quantum dots (QDs) through sub-10-nm electron-beam lithography (EBL).

The lithographically placement of individual QDs is one step towards the fabrication of excitonic circuits[38-40] and nano-optical devices[41] at the sub-10 nm scale. Furthermore, this technique enables the investigation of fundamental properties of QDs, such as energy transfer between lithographically-placed QDs.

3.1. Fabrication process

The fabrication process for QD placement is illustrated in Figure 3-1a. A poly(methylmethacrylate) (PMMA) resist was spin cast on a silicon substrate, and then the templating mask was fabricated by using the Raith150 EBL system at 30 keV. After defining the PMMA templates, a solution of QDs (6-nm-diameter CdSe) was spin casted and the remaining resist was removed by dissolution in acetone. This process resulted in QD clusters attached on the substrate. Figure 3-1b shows the PMMA patterning, which was optimized for minimum template (i.e., hole) size of 8 nm. The placed QDs were analyzed in a Zeiss scanning electron microscope (SEM) at 10 keV and 6 mm working distance.

In order to minimize the number of QDs in each cluster and increase pattern uniformity, the QD solution concentration, resist thickness, and feature size were optimized. In addition, the effect of QD ligand concentration in the fabrication process was investigated.

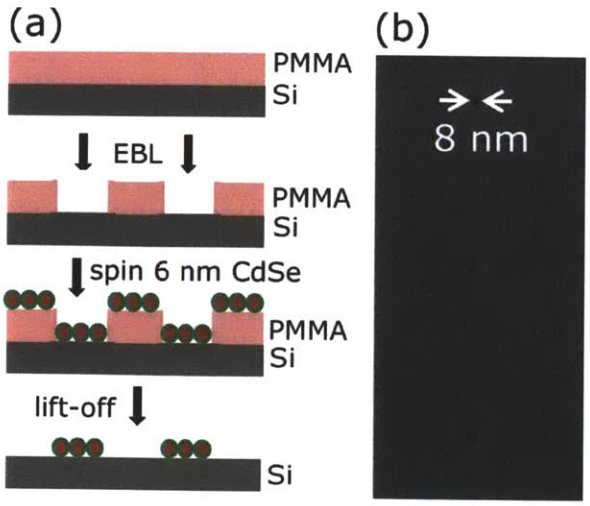

Figure 3-1. (a) Fabrication process of templated QDs. PMMA was spin coated to a thickness of 40 nm on Si, followed by EBL. Then, 6-nm-diameter CdSe QDs were spin coated. The PMMA lift off was done with acetone, leaving small clusters of CdSe QDs. (b) Scanning-electron micrographs of optimized PMMA templates with a minimum feature size of 8 nm for development at 7°C.

3.2. Process optimization

First, the concentration of colloidal QDs in solution was varied to investigate its effect on pattering resolution and pattern yield. Here the pattern yield was defined as the ratio of yielded QD clusters to designed QD clusters. Figure 3-2 shows QD patterning using 0.5 and 2 μM QD solutions. The solution with lower concentration provided small clusters (less than 10 QDs), but the pattern yield was only 25%. The solution with higher concentration provided 80% pattern yield, but with larger QD clusters than the ones obtained with the diluted solution. Therefore, the 2μM solution was chosen for the best yield performance and other parameters, such as template size and resist thickness, were optimized to decrease the number of QDs in each cluster.

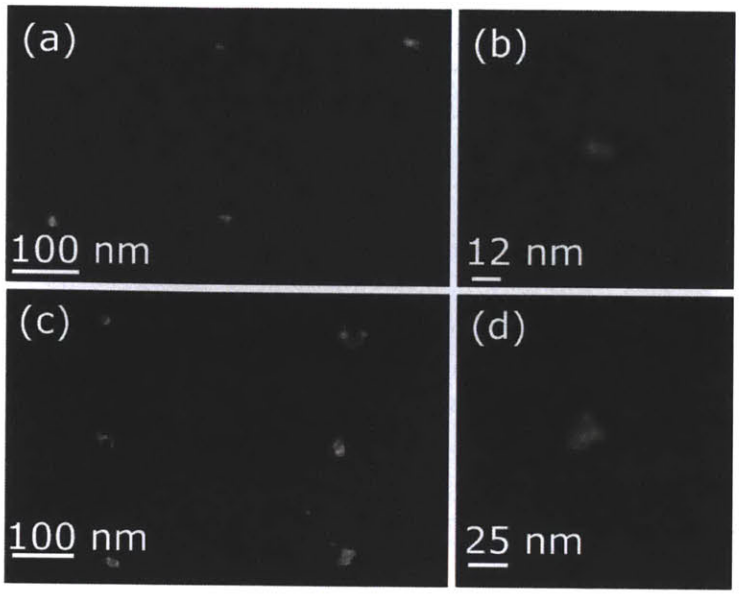

Figure 3-2. Scanning-electron micrographs of templated 6-nm-diameter CdSe QDs generated by a solution with low (0.5 μM) (a)-(b) and high (2 μM) (c)-(d) concentration of QDs. The PMMA mask used was 40 nm thick. In (a) the QD clusters have from one to 10 QDs, with 25% pattern yield. (b) shows a cluster with two QDs from the sample shown in (a). (c) has from three to 15 QDs in each cluster, with 80% pattern yield. (d) is a sub-10 QD cluster from the sample shown in (c).

To achieve the smallest QD clusters, the EBL process was optimized to decrease the size of templates. One technique to improve the resist contrast and decrease the minimum feature of PMMA is by carrying out the development at low temperature[12, 61].The samples were developed in IPA:MIBK (3:1) for 30 s and blown dry with nitrogen. The development temperature was varied from 0°C to 15°C, as shown in Figure 3-3. Minimum feature achieved at 0 and 7°C was 8 nm and at 15°C was 10 nm. Therefore, the temperature of 7°C was chosen to provide minimum template size for the QD placement process.

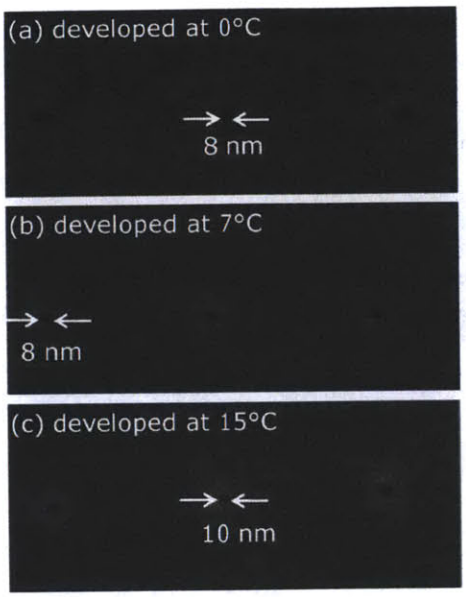

Figure 3-3. Scanning-electron micrographs of sub-10 nm holes in PMMA exposed by EBL at 30 keV, and developed for 30 s at: (a) 0°C; (b) 7°C; and (c) 15°C. (a) shows 8-9 nm holes. (b) has equal resolution than (a), and (c) shows larger features, i.e., 10-12 nm holes.

After the optimization of both solution concentration and development temperature, the resist thickness was varied to obtain the smallest QD clusters. Figure 3-2 shows patterning by using 40 nm thick PMMA as mask. The relatively thick resist creates a template with higher volume that accommodates and attracts more QDs per template.

In order to reduce the number of QDs in each cluster, a 12 nm thick PMMA was used instead. Figure 3-4 shows the results of the optimized process, by using 12-nm-thick PMMA as the mask, development temperature of 7°C, and 2μM of QD concentration. The QD clusters were successfully patterned at the desired position. Figure 3-4c shows the smallest QD clusters, were single QD, dimers and trimers were placed.

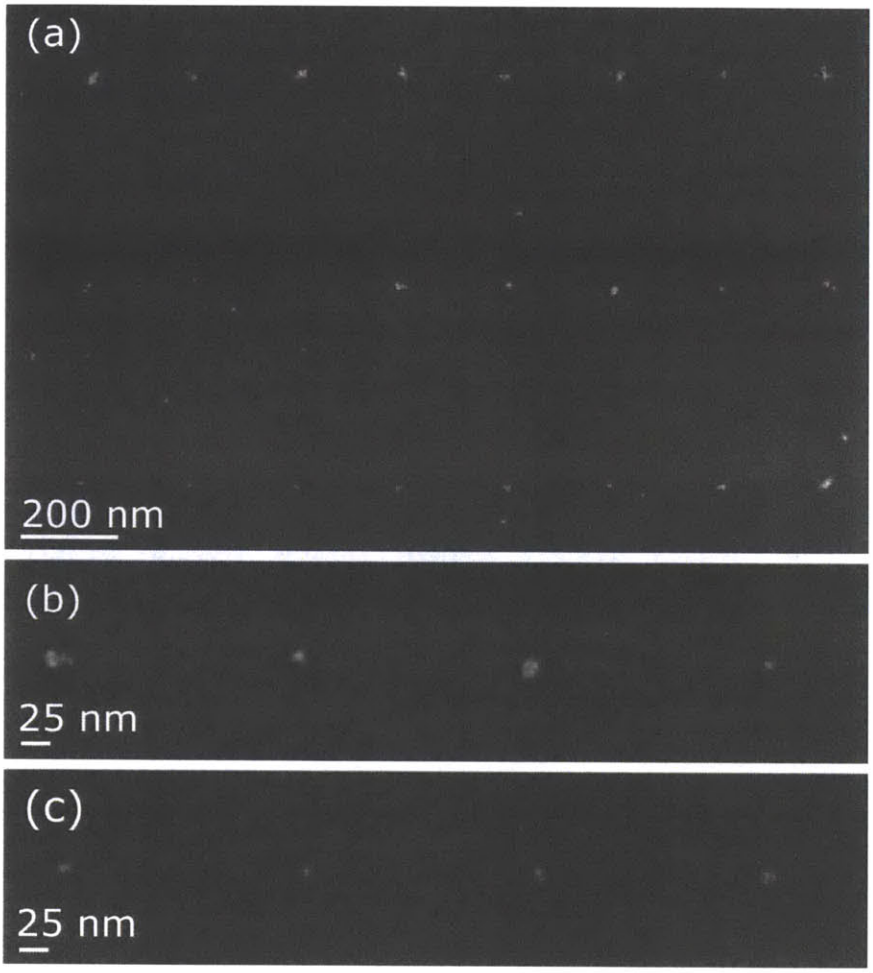

Figure 3-4. Scanning-electron micrographs of templated 6-nm-diameter CdSe QDs. The solution concentration was 2 μM. (a) shows an overview of the sample. There are a few QDs present outside the patterned area. These QDs were presumably re-deposited during the lift-off process. (b) and (c) are higher magnification of the middle and bottom rows of QDs shown in (a). Clusters with one QD were achieved.

Although Figure 3-4 shows small clusters of QDs, there is an evident statistical variation in the fabricated structure. Section 3.3 presents a statistical characterization of the placed QD clusters.

3.3. Statistical analysis

In the previous section, placement of QD was demonstrated with possibility to achieve single-QD placement. In order to quantify the statistical distribution of this process, a histogram of the fabricated structures is shown in figure 3-5.

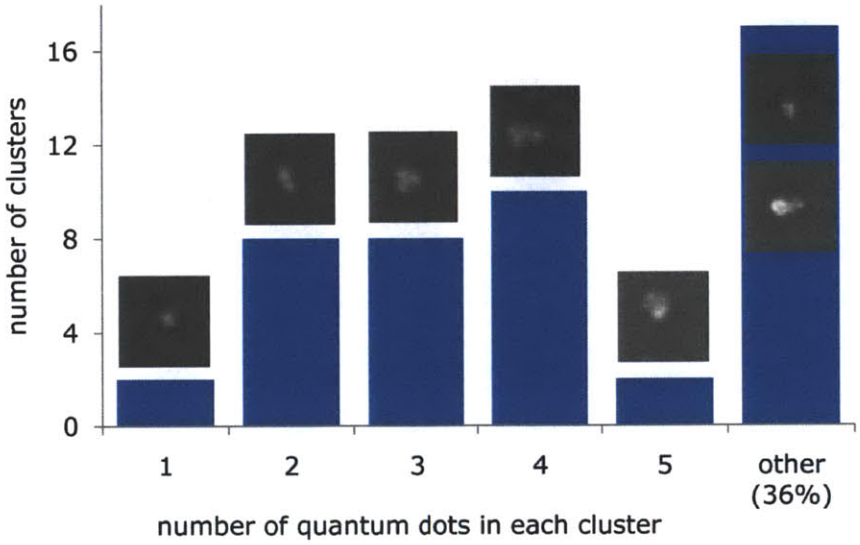

Figure 3-5. Histogram of the number of QDs (6-nm-diameter CdSe) in each cluster. The total number of analyzed clusters was 54. The QDs were counted visually by using high resolution SEM micrographs, obtained at 10 keV in a Zeiss SEM (Gemini column). Above every histogram bar is presented a typical SEM image used to count the QDs in a cluster.

The pattern yield, or the percentage of yielded structures, was 87%. The average number of QDs in each cluster was three. For this average value, only clusters with an identifiable number of QDs (64% of total) were considered. QD clusters with undetermined number of QDs were 36%. From these undetermined clusters, 24% (8% of total) had area smaller than 12×12 nm (2×2 dots), so they were expected to have less than 5 QDs in each cluster. 76% of the undetermined clusters (27% of total) had area bigger than 12×12 nm; so, they were expected to have more than 5 QDs in each cluster. The

difficulty in counting QDs lies in the SEM resolution limits and residues from PMMA and solvents (i.e., acetone, hexane) in the fabrication process.

3.4. Surface chemistry

For application of the templated QDs in excitonic or nano-optical devices, one would have to characterize its optical properties, such as the photoluminescence (PL) intensity and exciton lifetime. The CdSe QDs (or core QDs) are not optimized for PL experiments because they present dark surface states that do not emit, leading to decreased PL signal. Then, there is a need to investigate placement of core/shell dots, such as CdSe/CdZnS, to maximize QD PL and take advantage of its optical properties. The shell isolates the core from recombination centers that decrease exciton lifetime and the PL intensity[22]. One problem that arises by using different QDs is their distinct ligand composition[62].

The concentration of ligands on the QD surface was varied to investigate their effects on the placement process. The majority of the ligands were synthesized as phosphonic acid[62]. Quantifying the exact composition of ligands on a QD surface is still a challenge in the field, so its concentration is rather qualitative than a quantitative measure. Nevertheless, the ligand concentration was decreased by performing multiple purification processes in the QD solution therefore decreasing the phosphonic acid concentration.

Figure 3-6 shows an experiment to verify the QD attachment on 300 nm SiO_2 on top of Si. The SiO_2 layer was used to isolate the QDs from the bulk Si, avoiding PL quenching due to exciton energy transfer from the higher band gap (CdSe ~1.8 eV) to the lower band gap (Si ~1.1 eV) material. This substrate is also suitable for SEM metrology because the Si is conductive. Figure 3-6a and 3-6b present a sample with QDs that

received one purification[62] of the solution. Figure 3-6c and 3-6d present a sample with QDs that received three purification steps of the solution, therefore, had a lower concentration of the phosphonic acid ligand. The sample that received three purifications had no QD attachment problem after the acetone lift-off process, as shown in Figure 3-6d. Therefore, the reduced concentration of ligands promoted QD adhesion, which enables high pattern uniformity for placing CdSe/CdZnS QDs.

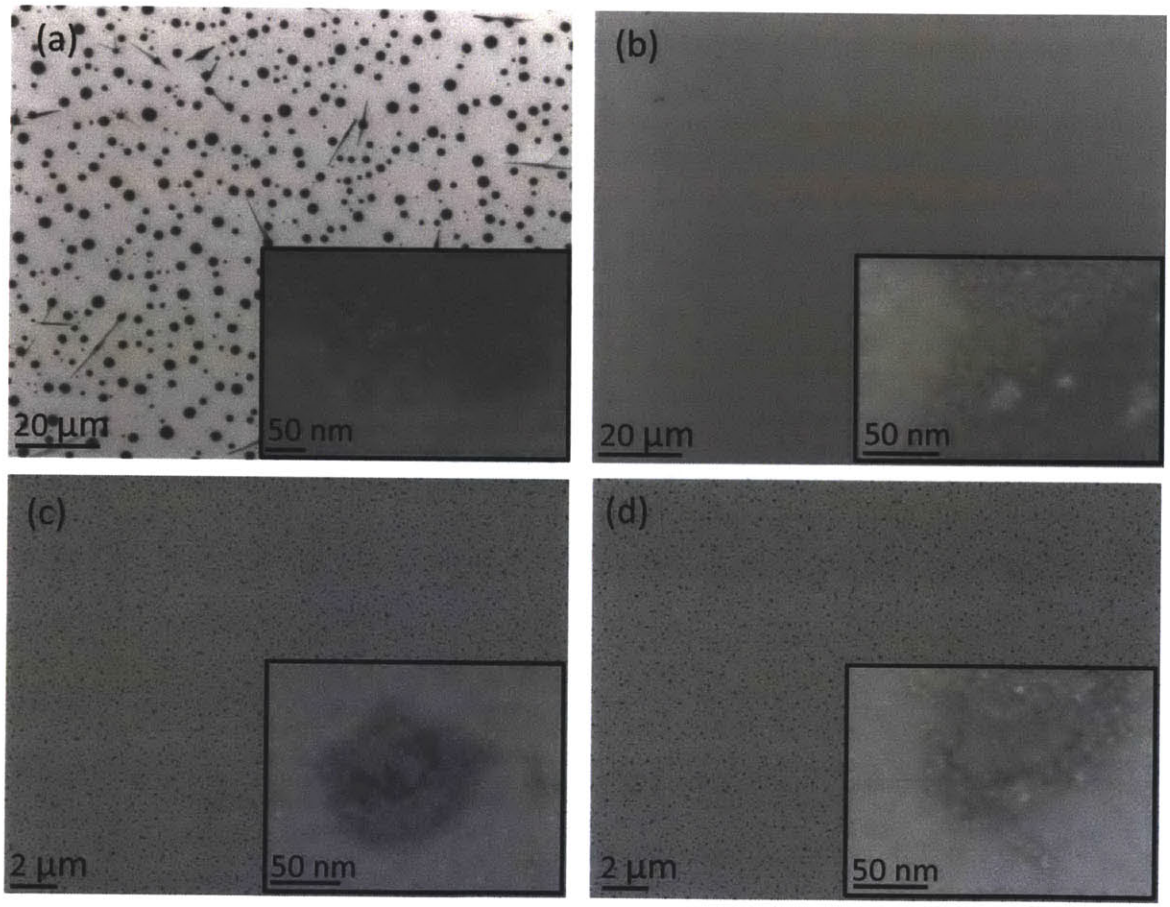

Figure 3-6. Scanning electron micrographs of 4-nm-diameter CdSe/CdZnS spun on SiO_2 substrates. (a) shows QDs purified one time[62] without further processing. (b) shows QDs as prepared in (a) followed by acetone dipping for 3 min to simulate the lift-off conditions of the QD-patterning process. (c) consists of QDs purified three times without further processing. (d) consists of QDs as prepared in (c) followed by acetone dipping for 3 min. The insets of all figures show higher magnification of the darker areas, which are QD agglomerations. The QD attachment after acetone processing is clearly improved with three

purification steps, which indicate the smaller concentration of ligands on QD surface favors its adhesion on the substrate.

The next step on this project is to template core/shell CdSe/CdZnS QDs to achieve placement of QDs with significant PL signal.

3.5. Summary

This chapter described a templated self-assembly technique to control the position of individual QDs through EBL. This QD-placement process allowed fabricating QD clusters with 1 to 5 QDs. The process was developed by optimizing QD solution concentration, resist thickness, and template size. One figure of merit in this process is the pattern yield, which is the ratio of yielded structures to the patterned templates. A pattern yield of 87% was achieved with an average of 3 QDs in each cluster. This optimized top-down lithographic process is a step towards the integration of individual QDs in optoelectronic systems.

Chapter 4. Future Work

This chapter describes future work planned to complement this thesis. First, this chapter describes preliminary optical characterization of placed colloidal quantum dots (QDs). Second, this chapter discusses the challenges of sub-5 nm patterning with an aberration-corrected scanning transmission electron microscope (STEM).

4.1. Quantum dot optical characterization

For application of the templated QDs in excitonic or nano-optical devices, one would have to characterize its optical properties. Key optical properties to be investigated are photoluminescence (PL) intensity, spectrum emission, and exciton lifetime.

Two different samples were prepared as described in chapter 3. Type-I sample contained patterned CdSe (6-nm diameter) core QDs. Type-II sample contained patterned CdSe/CdZnS core/shell (9-nm diameter) QDs. The substrates used for these samples were 300 nm SiO_2 on silicon. The main function of the silicon dioxide is isolating the QDs from the bulk Si, avoiding PL quenching due to exciton energy transfer from the higher band gap (CdSe ~1.8 eV) to the lower band gap (Si ~1.1 eV) material.

These samples of QDs were observed by confocal scanning microscopy using an air microscope objective (60×, 0.7 NA) and a 514 nm pulsed diode laser for excitation (2.5 MHz, ≈30 ps pulse width). The collected emission was detected by an avalanche photodiode-based single-photon detector.

The confocal PL of sample type-I is presented in Figure 4-1. The PL of the ensemble of QDs (depicted as the number '5') was resilient after the fabrication process. However, single-CdSe QD did not emit light. This assumption was verified because the CdSe QDs

were visible only in SEM and not in the PL setup. Therefore, there is a need for core/shell QDs to avoid exciton recombination centers from the surface, leading to higher luminescent QDs.

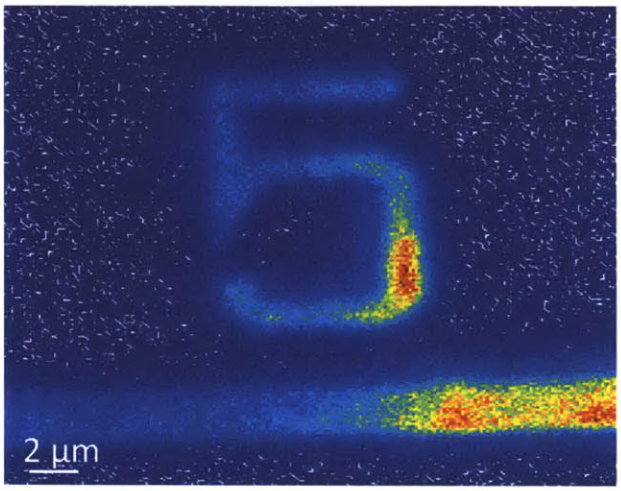

Figure 4-1. Confocal photoluminescence (PL) of CdSe QDs with 6 nm diameter. The peak of emission wavelength was 540 nm. This large area pattern maintained its PL even two weeks after the fabrication process, in ambient atmosphere. However, the sub-20-nm clusters of QDs did not presented PL.

The confocal PL of sample type-II is presented on Figure 4-2. Single CdSe/CdZnS (9-nm diameter) presented PL after the fabrication process. However, the QD attachment on the substrate was poorer than with core QDs. In addition, significant re-deposition of QDs during the lift-off in the fabrication process (described in chapter 3) lead to unwanted QDs in the unpatterned area. Nevertheless, these small clusters of QDs maintained PL, i.e., they were optically active after the fabrication process.

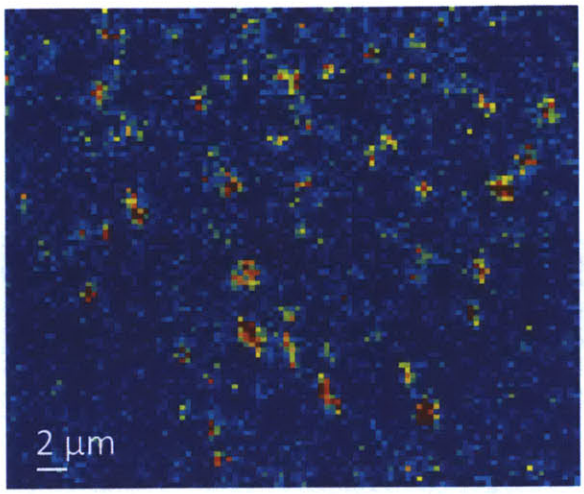

Figure 4-2. Confocal photoluminescence of CdSe/CdZnS QDs (core/shell with 4nm core) with 9 nm diameter. The peak of emission wavelength was 610 nm. These QDs were templated, but there was significant re-deposition of QDs.

Further work is still necessary to optimize the QD placement and maintaining optical quality, such as placing QDs with the chemical processing described in chapter 3, section 3.4.

4.2. Sub-5 nm STEM lithography

Chapter 2, at section 2.2, described electron-beam lithography using an aberration corrected scanning transmission electron microscope (STEM), i.e., STEM lithography. One key result was the achieved minimum feature size of 1 nm. However, further investigation is still necessary to achieve uniform 1-nm patterning. Figure 4-3 shows one attempt to increase feature size control, but new challenges need to be addressed.

Challenges associated with 1-nm patterning are resist collapse, resist adhesion and metrology. A 1-nm-diameter post or 1-nm-wide line, with 15 nm thick resist, does not have sufficient mechanical stability and tends to collapse during resist development. The

adhesion problem is intuitive since 1-nm features have small surface contact with the substrate and could be easily removed during development. The metrology challenge is due to small dimensions, only accessible with transmission electron microscope (TEM) or atomic force microscope (AFM).

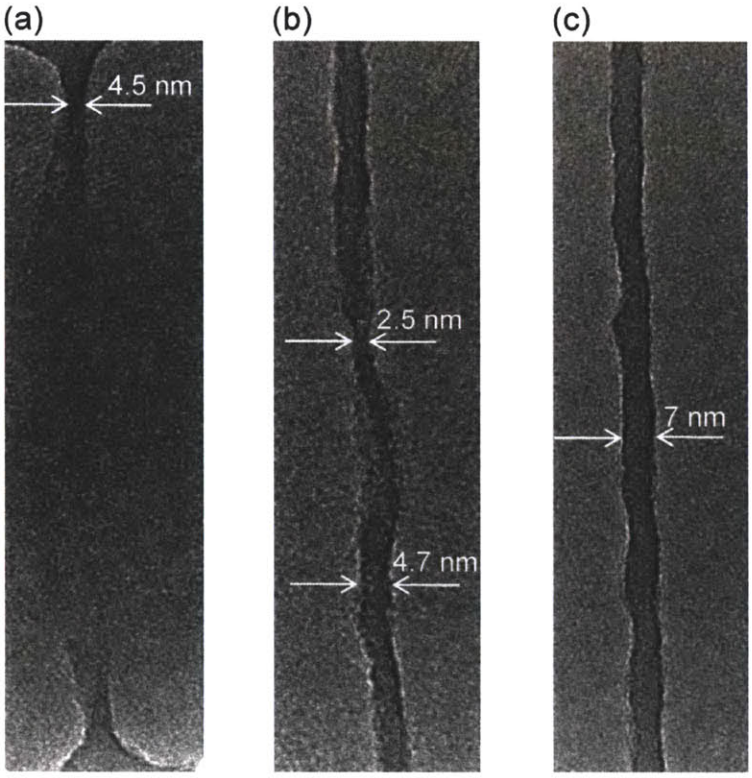

Figure 4-3. Bright field transmission electron micrograph of HSQ lines, exposed at 200 keV. The HSQ thickness was 20 nm and it was on top of a 50-nm-thick Si_3N_4 membrane. (a)-(c) had linear-dose of 16 nC/cm (10,000 electrons/nm), 28 nC/cm (17,000 electrons/nm), and 46 nC/cm (28,000 electrons/nm), respectively. The exposure step size was 2 nm. (a) did not receive enough dose in the entire line and collapsed. In addition, there is significant proximity effect generated by the exposed pads connected to the lines, indicated by the larger width at the beginning and end. (b) had non-uniform line-width, with 2.5 nm as minimum width at the center, presumably due to proximity effect. (c) had sufficient dose and better uniformity than (a) and (b).

One strategy to fabricate 1-nm features is by using collapsed structures[63]. Collapsed features (lines or posts) with 1 nm dimension pose a challenge for TEM metrology, because of poor signal-to-noise ratio between the structure and the supportive membrane. AFM metrology is also an option, but could suffer from membrane roughness and curvature. To overcome the TEM metrology problem, sub-10-nm thick Si_3N_4 membrane could be used to increase signal-to-noise ratio.

Another strategy for 1-nm patterning is attaching supportive structures on the features to avoid the structure collapse, as indicated in Figure 2-8 and schematically in Figure 4-4. Figure 4-4 presents large area pads to anchor the high-resolution grating. In addition, the grating interception (or corners) has larger area and stability to hold the lines. The structure should also be symmetric to suppress net-capillary forces during evaporation of the developer.

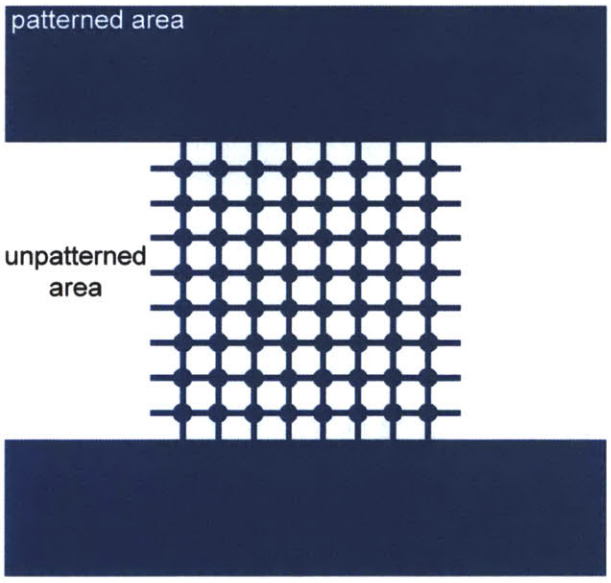

Figure 4-4. Schematic top-view of a structure to avoid collapse during development. Blue area represents the fabricate structure and the white background is the substrate. The large area pads and reinforced interconnects in this grating are designed to give mechanical stability to the thin lines that compose the square grating.

Bibliography

1. Grigorescu, A.; van der Krogt, M.; Hagen, C.; Kruit, P., 10 nm lines and spaces written in HSQ, using electron beam lithography. *Microelectronic Engineering* **2007,** 84, (5-8), 822-824.
2. Yang, J.; Berggren, K., Using high-contrast salty development of hydrogen silsesquioxane for sub-10-nm half-pitch lithography. *Journal of Vacuum Science & Technology B* **2007,** 25, (6), 2025-2029.
3. Cord, B.; Yang, J.; Duan, H.; Joy, D.; Klingfus, J.; Berggren, K., Limiting factors in sub-10 nm scanning-electron-beam lithography. *Journal of Vacuum Science & Technology B* **2009,** 27, (6), 2616-2621.
4. Yang, J.; Cord, B.; Duan, H.; Berggren, K.; Klingfus, J.; Nam, S.; Kim, K.; Rooks, M., Understanding of hydrogen silsesquioxane electron resist for sub-5-nm-half-pitch lithography. *Journal of Vacuum Science & Technology B* **2009,** 27, (6), 2622-2627.
5. Pease, R. F., To charge or not to charge: 50 years of lithographic choices. *J. Vac. Sci. Technol. B* **2010,** 28, (6), C6A1-C6A6.
6. Olkhovets, A.; Craighead, H., Low voltage electron beam lithography in PMMA. *Journal of Vacuum Science & Technology B* **1999,** 17, (4), 1366-1370.
7. Namatsu, H.; Yamaguchi, T.; Nagase, M.; Yamazaki, K.; Kurihara, K., Nano-patterning of a hydrogen silsesquioxane resist with reduced linewidth fluctuations. *Microelectronic Engineering* **1998,** 42, 331-334.
8. Fujita, J.; Ohnishi, Y.; Ochiai, Y.; Matsui, S., Ultrahigh resolution of calixarene negative resist in electron beam lithography. *Applied Physics Letters* **1996,** 68, (9), 1297-1299.
9. Broers, A.; Molzen, W.; Cuomo, J.; Wittels, N., Electron-beam fabrication of 80-a metal structures. *Applied Physics Letters* **1976,** 29, (9), 596-598.
10. Howard, R.; Craighead, H.; Jackel, L.; Mankiewich, P.; Feldman, M., Electron-beam lithography from 20 to 120 kev with a high-quality beam. *Journal of Vacuum Science & Technology B* **1983,** 1, (4), 1101-1104.
11. Yang, X.; Xiao, S.; Wu, W.; Xu, Y.; Mountfield, K.; Rottmayer, R.; Lee, K.; Kuo, D.; Weller, D., Challenges in 1 Teradot/in.(2) dot patterning using electron beam lithography for bit-patterned media. *Journal of Vacuum Science & Technology B* **2007,** 25, (6), 2202-2209.
12. Hu, W.; Sarveswaran, K.; Lieberman, M.; Bernstein, G., Sub-10 nm electron beam lithography using cold development of poly(methylmethacrylate). *Journal of Vacuum Science & Technology B* **2004,** 22, (4), 1711-1716.
13. Kyser, D.; Viswanathan, N., Monte-carlo simulation of spatially distributed beams in electron-beam lithography. *Journal of Vacuum Science & Technology* **1975,** 12, (6), 1305-1308.
14. Murata, K.; Kyser, D.; Ting, C., Monte-carlo simulation of fast secondary-electron production in electron-beam resists. *Journal of Applied Physics* **1981,** 52, (7), 4396-4405.
15. Joy, D.; Luo, S., An empirical stopping power relationship for low-energy electrons. *Scanning* **1989,** 11, (4), 176-180.
16. Duan, H.; Manfrinato, V.; Yang, J.; Winston, D.; Cord, B.; Berggren, K., Metrology for electron-beam lithography and resist contrast at the sub-10 nm scale. *Journal of Vacuum Science & Technology B* **2010,** 28, (6), C6H11-C6H17.
17. Zhu, Y.; Inada, H.; Nakamura, K.; Wall, J., Imaging single atoms using secondary electrons with an aberration-corrected electron microscope. *Nature Materials* **2009,** 8, (10), 808-812.
18. Scholes, G.; Rumbles, G., Excitons in nanoscale systems (vol 5, pg 683, 2006). *Nature Materials* **2006,** 5, (11), 920-920.
19. Ozbay, E., Plasmonics: Merging photonics and electronics at nanoscale dimensions. *Science* **2006,** 311, (5758), 189-193.
20. Novotny, L.; van Hulst, N., Antennas for light. *Nature Photonics* **2011,** 5, (2), 83-90.
21. Alivisatos, A., Semiconductor clusters, nanocrystals, and quantum dots. *Science* **1996,** 271, (5251), 933-937.
22. Empedocles, S.; Norris, D.; Bawendi, M., Photoluminescence spectroscopy of single CdSe nanocrystallite quantum dots. *Abstracts of Papers of the American Chemical Society* **1997,** 213, 10-PHYS.
23. Koole, R.; Liljeroth, P.; Donega, C.; Vanmaekelbergh, D.; Meijerink, A., Electronic coupling and exciton energy transfer in CdTe quantum-dot molecules. *Journal of the American Chemical Society* **2006,** 128, (32), 10436-10441.
24. Zhang, Q.; Atay, T.; Tischler, J.; Bradley, M.; Bulovic, V.; Nurmikko, A., Highly efficient resonant coupling of optical excitations in hybrid organic/inorganic semiconductor nanostructures. *Nature Nanotechnology* **2007,** 2, (9), 555-559.
25. Choi, J.; Luria, J.; Hyun, B.; Bartnik, A.; Sun, L.; Lim, Y.; Marohn, J.; Wise, F.; Hanrath, T., Photogenerated Exciton Dissociation in Highly Coupled Lead Salt Nanocrystal Assemblies. *Nano Letters* **2010,** 10, (5), 1805-1811.
26. Nair, G.; Chang, L.; Geyer, S.; Bawendi, M., Perspective on the Prospects of a Carrier Multiplication Nanocrystal Solar Cell. *Nano Letters* **2011,** 11, (5), 2145-2151.
27. Anikeeva, P.; Halpert, J.; Bawendi, M.; Bulovic, V., Quantum Dot Light-Emitting Devices with Electroluminescence Tunable over the Entire Visible Spectrum. *Nano Letters* **2009,** 9, (7), 2532-2536.
28. Ratchford, D.; Shafiei, F.; Kim, S.; Gray, S.; Li, X., Manipulating Coupling between a Single Semiconductor Quantum Dot and Single Gold Nanoparticle. *Nano Letters* **2011,** 11, (3), 1049-1054.

29. Liddle, J.; Cui, Y.; Alivisatos, P., Lithographically directed self-assembly of nanostructures. *Journal of Vacuum Science & Technology B* **2004,** 22, (6), 3409-3414.
30. Cui, Y.; Bjork, M.; Liddle, J.; Sonnichsen, C.; Boussert, B.; Alivisatos, A., Integration of colloidal nanocrystals into lithographically patterned devices. *Nano Letters* **2004,** 4, (6), 1093-1098.
31. Liu, S.; Maoz, R.; Sagiv, J., Planned nanostructures of colloidal gold via self-assembly on hierarchically assembled organic bilayer template patterns with in-situ generated terminal amino functionality. *Nano Letters* **2004,** 4, (5), 845-851.
32. Xu, K.; Qin, L.; Heath, J., The crossover from two dimensions to one dimension in granular electronic materials. *Nature Nanotechnology* **2009,** 4, (6), 368-372.
33. Kramer, R.; Pholchai, N.; Sorger, V.; Yim, T.; Oulton, R.; Zhang, X., Positioning of quantum dots on metallic nanostructures. *Nanotechnology* **2010,** 21, (14), -.
34. Pattantyus-Abraham, A.; Qiao, H.; Shan, J.; Abel, K.; Wang, T.; van Veggel, F.; Young, J., Site-Selective Optical Coupling of PbSe Nanocrystals to Si-Based Photonic Crystal Microcavities. *Nano Letters* **2009,** 9, (8), 2849-2854.
35. Zhang, Q.; Dang, C.; Urabe, H.; Wang, J.; Sun, S.; Nurmikko, A., Large ordered arrays of single photon sources based on II-VI semiconductor colloidal quantum dot. *Optics Express* **2008,** 16, (24), 19592-19599.
36. Zhao, Y.; Thorkelsson, K.; Mastroianni, A.; Schilling, T.; Luther, J.; Rancatore, B.; Matsunaga, K.; Jinnai, H.; Wu, Y.; Poulsen, D.; Frechet, J.; Alivisatos, A.; Xu, T., Small-molecule-directed nanoparticle assembly towards stimuli-responsive nanocomposites. *Nature Materials* **2009,** 8, (12), 979-985.
37. Curto, A.; Volpe, G.; Taminiau, T.; Kreuzer, M.; Quidant, R.; van Hulst, N., Unidirectional Emission of a Quantum Dot Coupled to a Nanoantenna. *Science* **2010,** 329, (5994), 930-933.
38. High, A.; Novitskaya, E.; Butov, L.; Hanson, M.; Gossard, A., Control of exciton fluxes in an excitonic integrated circuit. *Science* **2008,** 321, (5886), 229-231.
39. Perdomo, A.; Vogt, L.; Najmaie, A.; Aspuru-Guzik, A., Engineering directed excitonic energy transfer. *Applied Physics Letters* **2010,** 96, (9), -.
40. Rebentrost, P.; Stopa, M.; Aspuru-Guzik, A., Forster Coupling in Nanoparticle Excitonic Circuits. *Nano Letters* **2010,** 10, (8), 2849-2856.
41. Akimov, A.; Mukherjee, A.; Yu, C.; Chang, D.; Zibrov, A.; Hemmer, P.; Park, H.; Lukin, M., Generation of single optical plasmons in metallic nanowires coupled to quantum dots. *Nature* **2007,** 450, (7168), 402-406.
42. Lee, Y.; Browning, R.; Maluf, N.; Owen, G.; Pease, R., Low-voltage alternative for electron-beam lithography. *Journal of Vacuum Science & Technology B* **1992,** 10, (6), 3094-3098.
43. Tilke, A.; Vogel, M.; Simmel, F.; Kriele, A.; Blick, R.; Lorenz, H.; Wharam, D.; Kotthaus, J., Low-energy electron-beam lithography using calixarene. *Journal of Vacuum Science & Technology B* **1999,** 17, (4), 1594-1597.
44. Rio, D.; Constancias, C.; Martin, M.; Icard, B.; van Nieuwstadt, J.; Vijverberg, J.; Pain, L., 5 kV multielectron beam lithography: MAPPER tool and resist process characterization. *Journal of Vacuum Science & Technology B* **2010,** 28, (6), C6C14-C6C20.
45. Muray, L.; Silver, C.; Spallas, J., Sub-100-nm lithography with miniature electron beam columns. *Journal of Vacuum Science & Technology B* **2006,** 24, (6), 2945-2950.
46. Lercel, M.; Craighead, H.; Parikh, A.; Seshadri, K.; Allara, D., Sub-10 nm lithography with self-assembled monolayers. *Applied Physics Letters* **1996,** 68, (11), 1504-1506.
47. Peuker, M., Optimum energy for high resolution low voltage electron beam lithography - Monte Carlo simulations and experiments. *Microelectronic Engineering* **2000,** 53, (1-4), 337-340.
48. Mohammad, M.; Fito, T.; Chen, J.; Buswell, S.; Aktary, M.; Stepanova, M.; Dew, S., Systematic study of the interdependence of exposure and development conditions and kinetic modelling for optimizing low-energy electron beam nanolithography. *Microelectronic Engineering* **2010,** 87, (5-8), 1104-1107.
49. Jamieson, A.; Willson, C.; Hsu, Y.; Brodie, A., A hydrogen silsesquioxane bilayer resist process for low-voltage electron beam lithography. *Advances in Resist Technology and Processing Xix, Pts 1 and 2* **2002,** 4690, 1171-1179.
50. Ghanbari, R. A. Physics and fabrication of quasi-one-dimensional conductors. Ph D, Massachusetts Institute of Technology, 1993.
51. Rishton, S.; Kern, D., Point exposure distribution measurements for proximity correction in electron-beam lithography on a sub-100 nm scale. *Journal of Vacuum Science & Technology B* **1987,** 5, (1), 135-141.
52. Chang, T., Proximity effect in electron-beam lithography. *Journal of Vacuum Science & Technology* **1975,** 12, (6), 1271-1275.
53. Manfrinato, V. R.; Cheong, L. L.; Duan, H.; Winston, D.; Smith, H. I.; Berggren, K. K., Sub-5 keV electron-beam lithography in hydrogen silsesquioxane resist. In Microelectronic Engineering: 2011.
54. Cheong, L. L. Low-voltage spatial-phase-locked scanning-electron-beam lithography. S m, Massachusetts Institute of Technology, 2010.
55. Smith, H., A statistical-analysis of ultraviolet, x-ray, and charged-particle lithographies. *Journal of Vacuum Science & Technology B* **1986,** 4, (1), 148-153.
56. L. Battistella, D. W., J. Ferrera, M.K. Mondol, Karl K. Berggren, The point exposure distribution. In Personal Communication: 2010.

57. Vieu, C.; Carcenac, F.; Pepin, A.; Chen, Y.; Mejias, M.; Lebib, A.; Manin-Ferlazzo, L.; Couraud, L.; Launois, H., Electron beam lithography: resolution limits and applications. *Applied Surface Science* **2000,** 164, 111-117.
58. Yasin, S.; Hasko, D.; Carecenac, F., Nanolithography using ultrasonically assisted development of calixarene negative electron beam resist. *Journal of Vacuum Science & Technology B* **2001,** 19, (1), 311-313.
59. Muray, A.; Scheinfein, M.; Isaacson, M.; Adesida, I., Radiolysis and resolution limits of inorganic halide resists. *Journal of Vacuum Science & Technology B* **1985,** 3, (1), 367-372.
60. Goldstein, J., *Scanning electron microscopy and x-ray microanalysis*. 3rd ed.; Kluwer Academic/Plenum Publishers: New York, 2003; p xix, 689 p.
61. Cord, B.; Lutkenhaus, J.; Berggren, K., Optimal temperature for development of poly(methylmethacrylate). *Journal of Vacuum Science & Technology B* **2007,** 25, (6), 2013-2016.
62. Murray, C.; Norris, D.; Bawendi, M., Synthesis and characterization of nearly monodisperse CdE (E = E, SE, Te) semiconductor nanocrystallites. *Journal of the American Chemical Society* **1993,** 115, (19), 8706-8715.
63. Duan, H.; Berggren, K., Directed Self-Assembly at the 10 nm Scale by Using Capillary Force-Induced Nanocohesion. *Nano Letters* **2010,** 10, (9), 3710-3716.